Supporting Information

MoS$_2$ oxidative etching caught in the act: Formation of single (MoO$_3$)$_n$ molecules.

Saeed Sovizi[a], Sergio Tosoni[b] and Robert Szoszkiewicz*[a]*

[a] Faculty of Chemistry, Biological and Chemical Research Centre, University of Warsaw, Żwirki i Wigury 101, 02-089 Warsaw, Poland

[b] Dipartimento di Scienza dei materiali, Università di Milano Bicocca, via Roberto Cozzi 55, 20125 Milano, Italy

To whom correspondence should be addressed: rszoszkiewicz@chem.uw.edu.pl (experiments)

or sergio.tosoni@unimib.it (simulations).

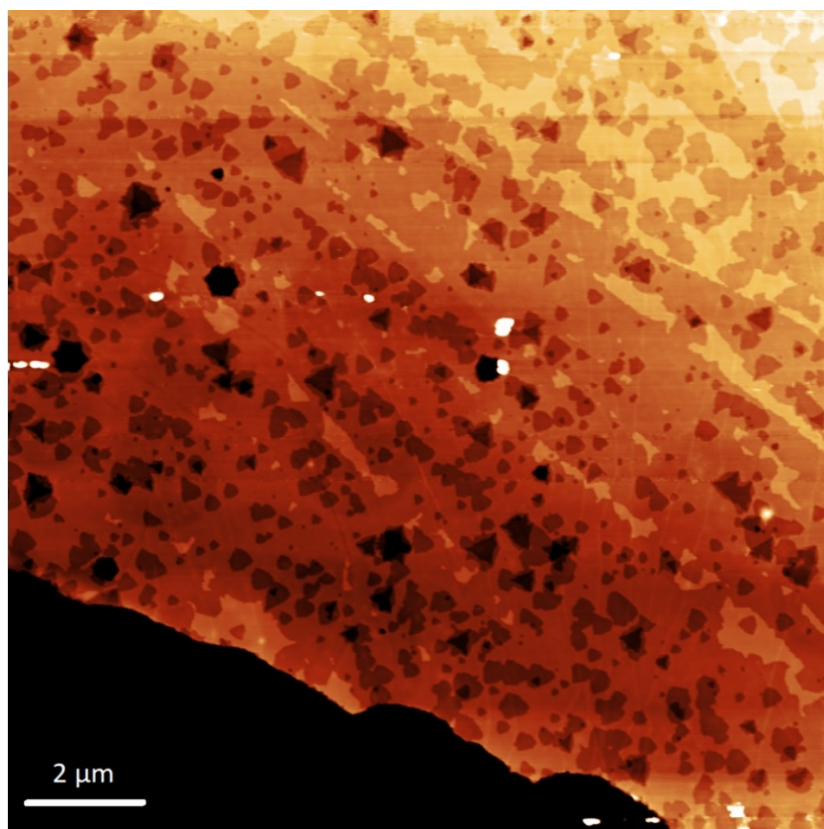**Additional AFM topography results:**

Fig. S1. High resolution 14 x 14 μm^2 NC-AFM topography of the same region of the Fig. 1(a) in the main paper after rastering the whole area in a contact-mode AFM. Image Z-scale is 5.6 nm. Brighter colors represent higher Z-scale.
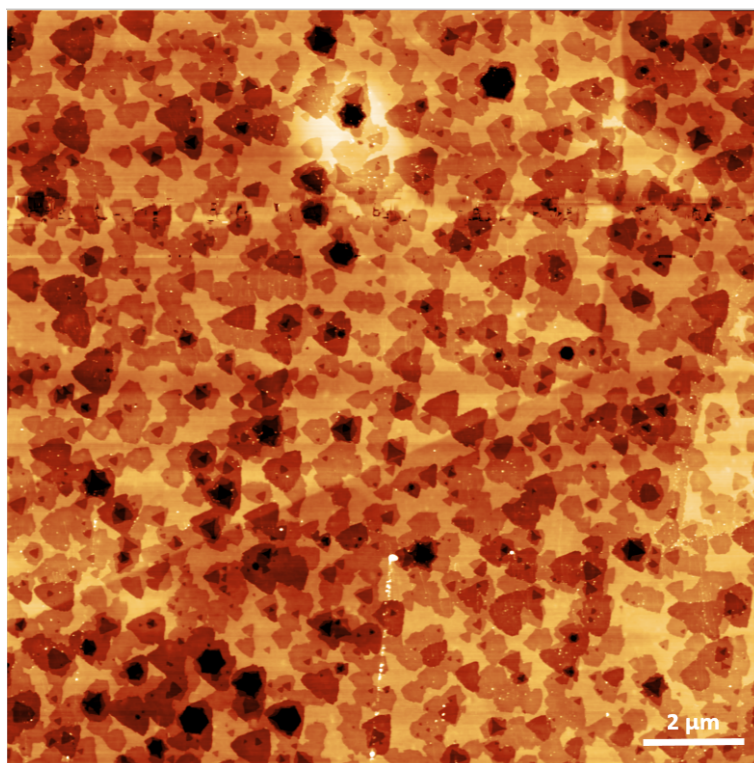

Fig. S2. High resolution 15 x 15 μm^2 NC-AFM topography of the second sample with a single MoS$_2$ flake thermally etched/oxidized at 370 °C for 15 minutes. Image Z-scale is 5 nm. Brighter colors represents higher Z-scale.
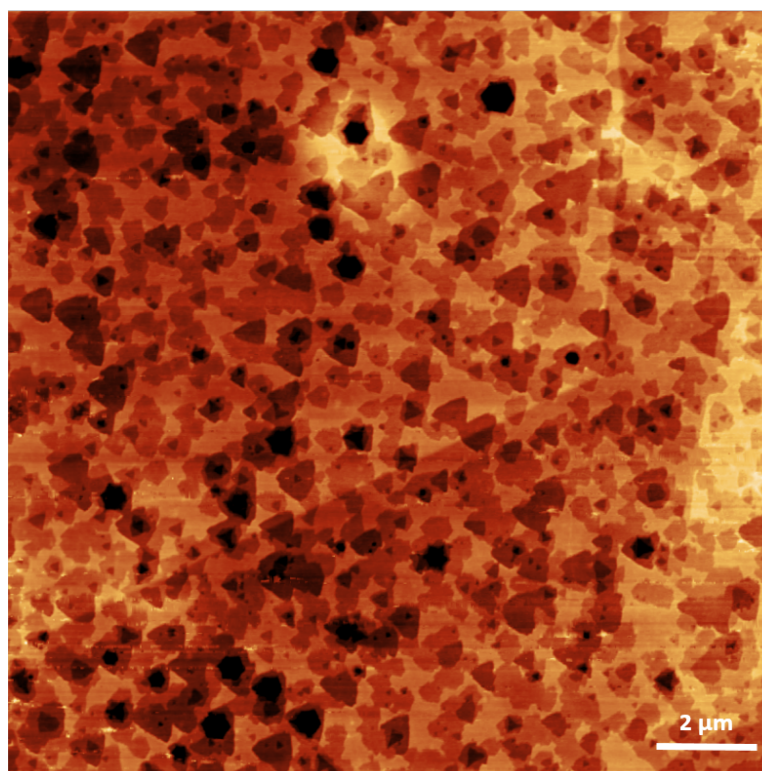
Fig. S3. High resolution 15.5 x 15.5 µm² NC-AFM topography from same area as in Fig. S2 after rastering in a contact-mode AFM. Image Z-scale is 5 nm. Brighter colors represents higher Z-scale.
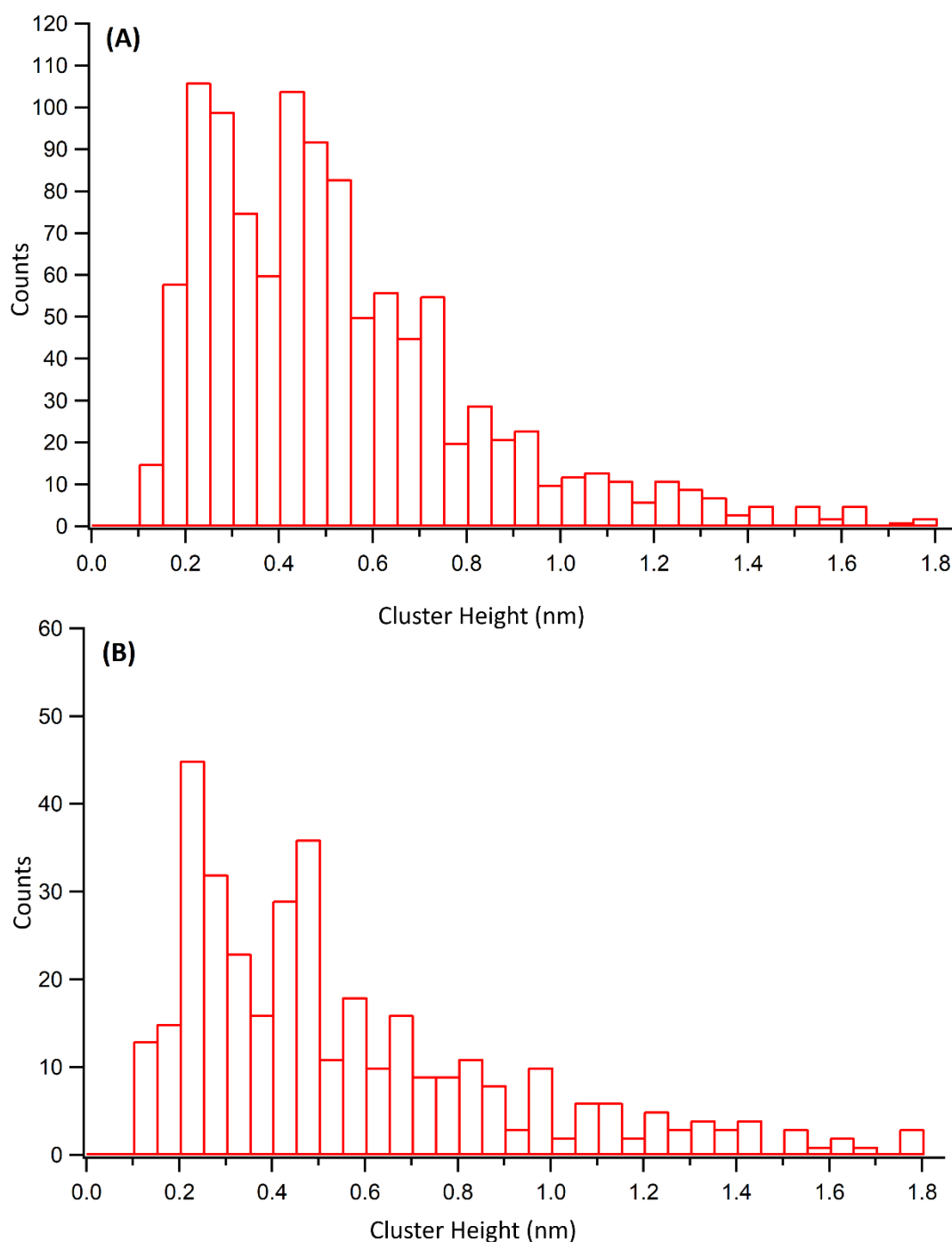

Fig. S4. (a) Height histogram of more than 1100 movable oxide clusters which were randomly chosen from sample 1 in Fig. 1 (a). The bin size is 0.05 nm. Single Gaussian fit: **0.391 ± 0.019 nm** / double Gaussian fit: **0.236 ± 0.007 nm, 0.475 ± 0.021 nm**. (b) Height histogram of more than 350 movable oxide clusters which were randomly chosen from sample 2 in Fig. S2. The bin size is 0.05 nm. Single Gaussian fit: **0.362 ± 0.026 nm** / double Gaussian fit: **0.236 ± 0.007 nm, 0.438 ± 0.031 nm**. The second peak position is different in parts (a) and (b). However, they are the same when considering errors. To understand this one

must appreciate that an error for each bin scales with the square root of the counts. Therefore, summing up the overall data from these two histograms is expected to decrease an overall error, see the main manuscript.

Gaussian fitting of the histograms

Two Gaussian fits (Eqs. S2 & S3) were used to find the peaks of cluster height histograms in Fig. 2 (main paper). Their optimized parameters obtained by Igor Pro 6.37 program (WaveMetrics, Inc., Lake Oswego, Oregon, USA) are shown in **Table S1**.

Single Gaussian fit:
$$y = y_0 + A_1\, exp\left\{ -\left(\frac{x - x_1}{d_1}\right)^2 \right\}$$
Eq. S2

Double Gaussian fit:
$$y = y_0 + A_1 exp\left\{ -\left(\frac{x - x_1}{d_1}\right)^2 \right\} + A_2\, exp\left\{ -\left(\frac{x - x_2}{d_2}\right)^2 \right\}$$
Eq. S3

Table S1. Optimized parameters for Gaussian fitting to Fig. 2.

Gaussian fit type	χ^2	y_0	A_1	x_1 (nm)	d_1 (nm)	A_2	x_2 (nm)	d_2 (nm)
Single	13016	9 ± 5	112 ± 10	0.405 ± 0.020	0.29 ± 0.3	-	-	-
Double	4486	9 ± 3	105 ± 16	0.236 ± 0.006	0.06 ± 0.01	99 ± 7	0.472 ± 0.021	0.26 ± 0.03

Additional DFT simulation results:

$(Mo_1O_3)/Mo_{1-x}S_{2-x}$
Height = 0.222 nm
$E_F = -2.90\ eV$

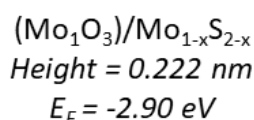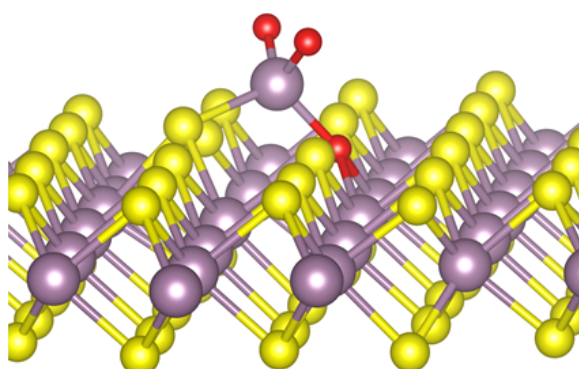**Fig. S5**. Calculated structure of $(Mo_1O_3)/Mo_{1-x}S_{2-x}$ where the Mo atom has been extracted from the basal plane.

Table S2. Formation energies of M_2O_4 and M_2O_6 from their monomers (MoO_2 and MoO_3) calculated by DFT at pristine and defective MoS_2 surfaces.

Reaction	Description	Formation

		energy (eV)
$(Mo_1O_2/MoS_2) + (Mo_1O_2/MoS_{2-x}) \rightarrow Mo_2O_4/MoS_{2-x}$	A MoO$_2$ monomer on pristine surface migrates to a MoO$_2$ monomer at the defect site to form a Mo$_2$O$_4$ dimer at sulfur vacancy	**-2.84**
$(Mo_1O_2/MoS_2) + (Mo_1O_2/MoS_{2-x}) \rightarrow Mo_2O_4/MoS_2$	A MoO$_2$ monomer on sulfur vacancy migrates to a MoO$_2$ monomer at the pristine MoS$_2$ surface to form a Mo$_2$O$_4$ dimer at perfect surface	**-1.41**
$(Mo_1O_3/MoS_2) + (Mo_1O_3/MoS_{2-x}) \rightarrow Mo_2O_6/MoS_{2-x}$	A MoO$_3$ monomer on pristine surface migrates to a MoO$_3$ monomer at the defect site to form a Mo$_2$O$_6$ dimer at sulfur vacancy	**-2.19**
$(Mo_1O_3/MoS_2) + (Mo_1O_3/MoS_{2-x}) \rightarrow Mo_2O_6/MoS_2$	A MoO$_3$ monomer on sulfur vacancy migrates to a MoO$_3$ monomer at the pristine MoS$_2$ surface to form a Mo$_2$O$_6$ dimer at perfect surface	**-0.51**

As seen in Table S2, formation of dimers are energetically favorable for both considered oxides (MoO$_2$ and MoO$_3$), however, MoO$_2$ were not detected within our studies. Moreover, a process when a monomer migrates and combines with its counterpart at a defect site is strongly preferred.

Detailed Raman studies on modified MoS$_2$ flakes:
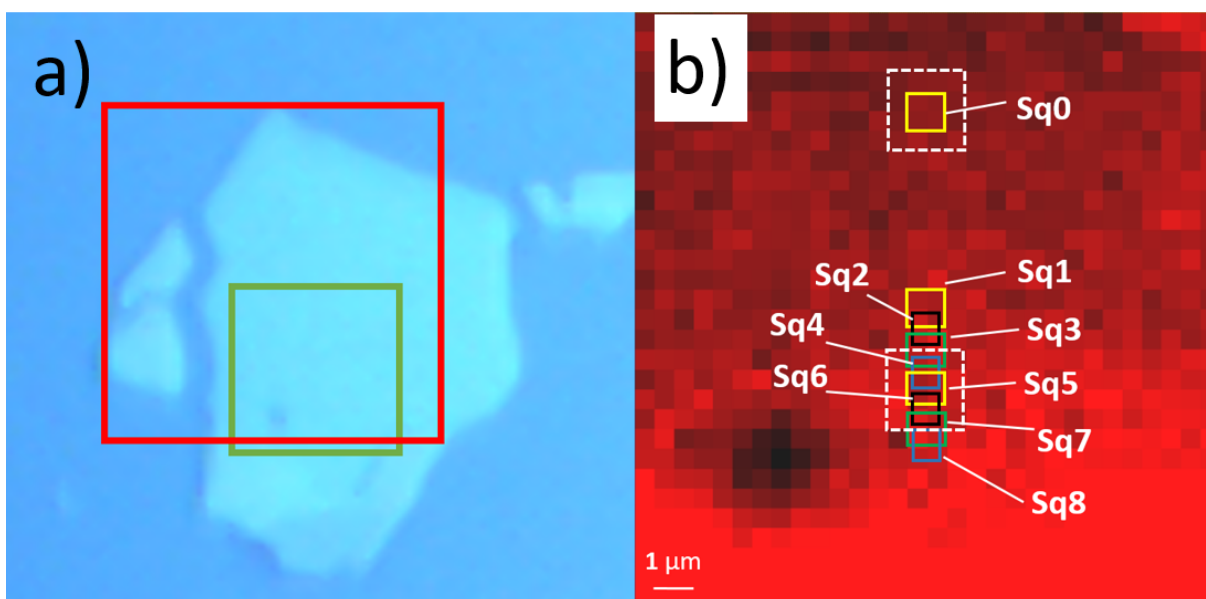
Fig. S6. (a) Optical image of the investigated flake. A red box shows the area of figure 4(b) from the main paper. (b) Raman map of a 15x15 µm^2 area depicted by a green box in (a). The map displays intensity of Raman shifts between 800 to 900 cm$^-$

[1]. The data was normalized by setting Si peak intensity at 520.35 cm^{-1} to 100 for all data points. Nine 2x2 pixels solid boxes (Sq0..Sq8) and two 4x4 pixels dashed-line boxes are marked for further analyses.
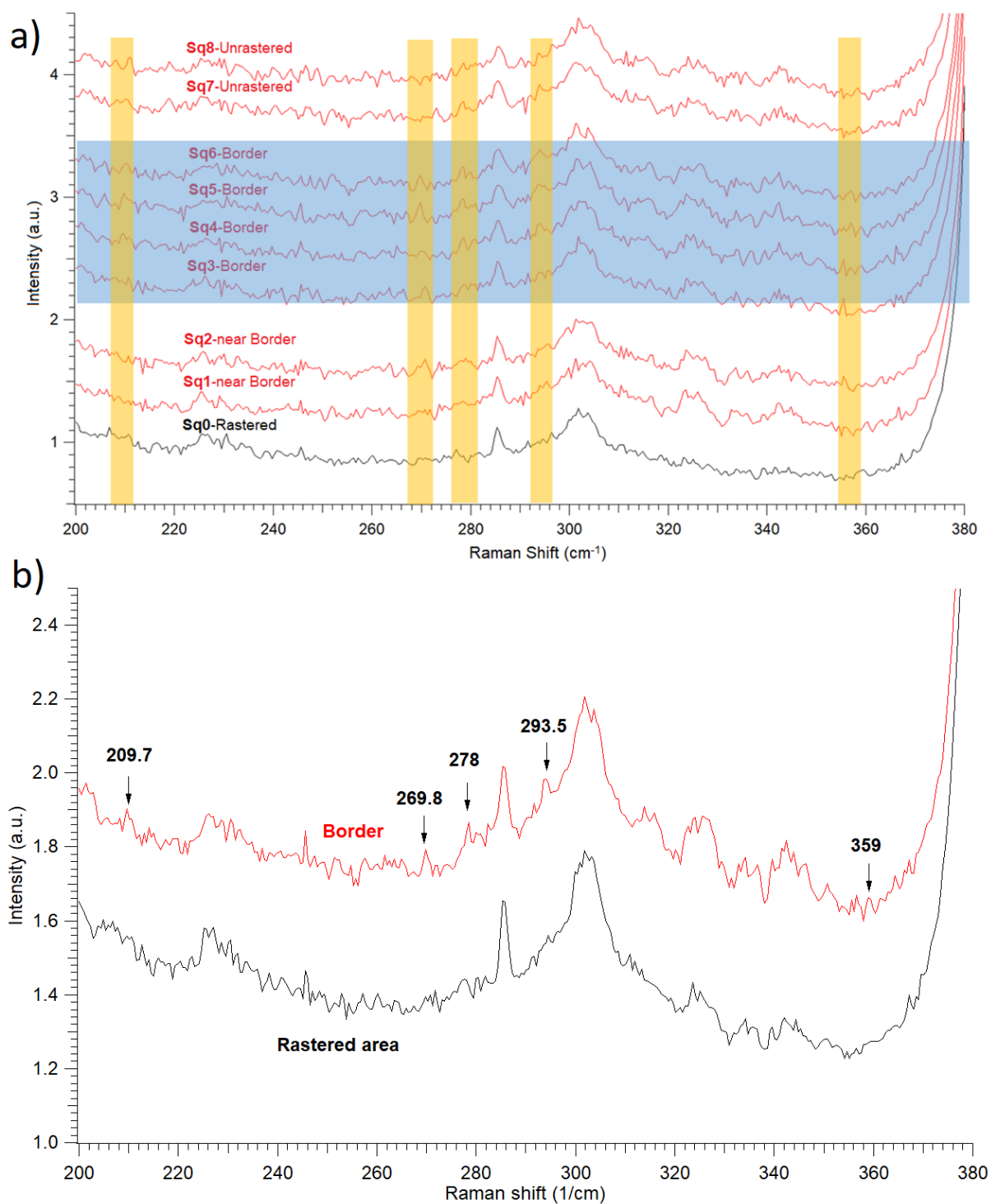
Fig. S7. Averaged Raman spectra of (a) 2x2 and (b) 4x4 boxes in the Raman shifts between 200 to 350 cm^{-1}.
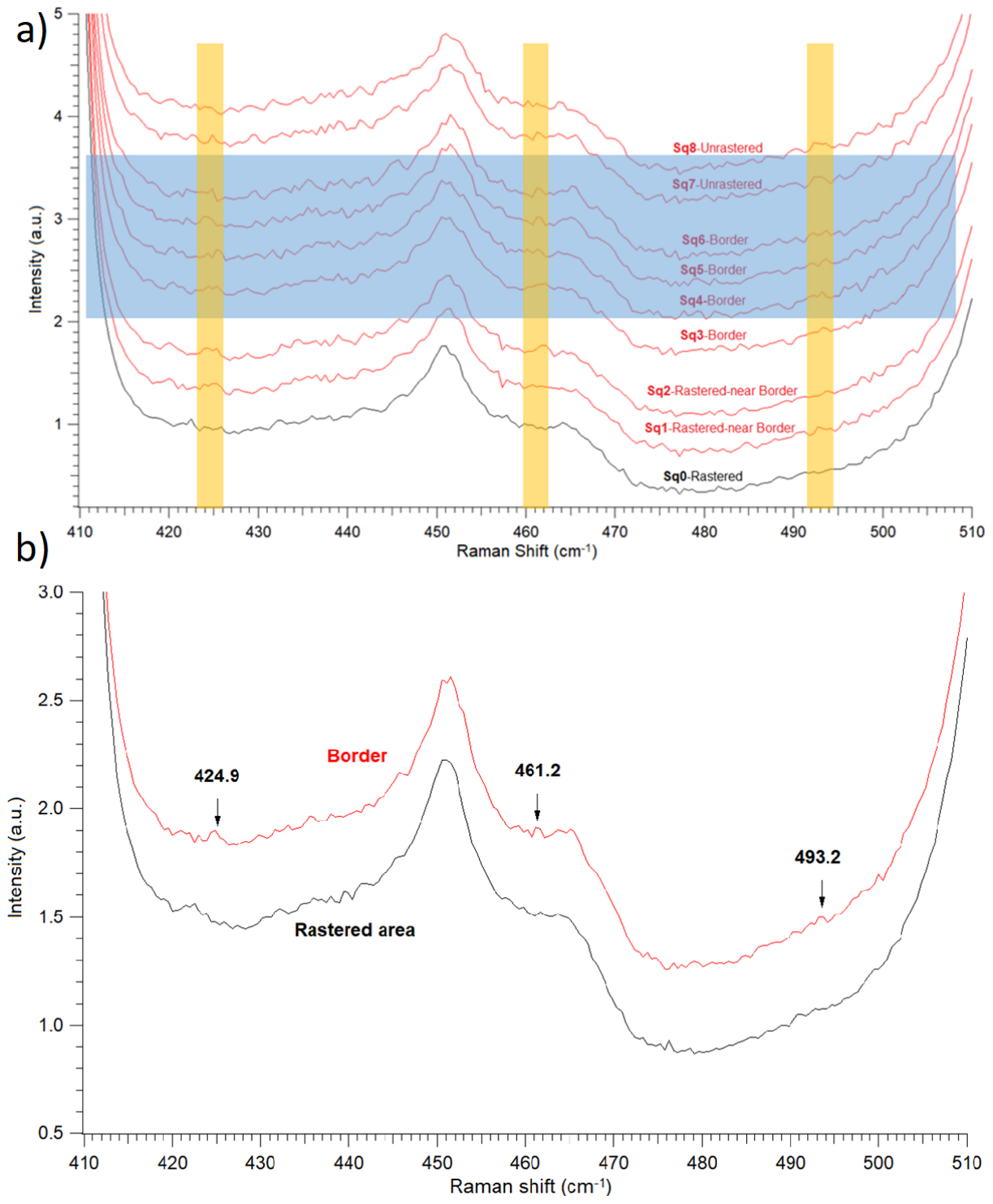
Fig. S8. Averaged Raman spectra of (a) 2x2 and (b) 4x4 boxes in the Raman shifts between 410 to 510 cm^{-1}.

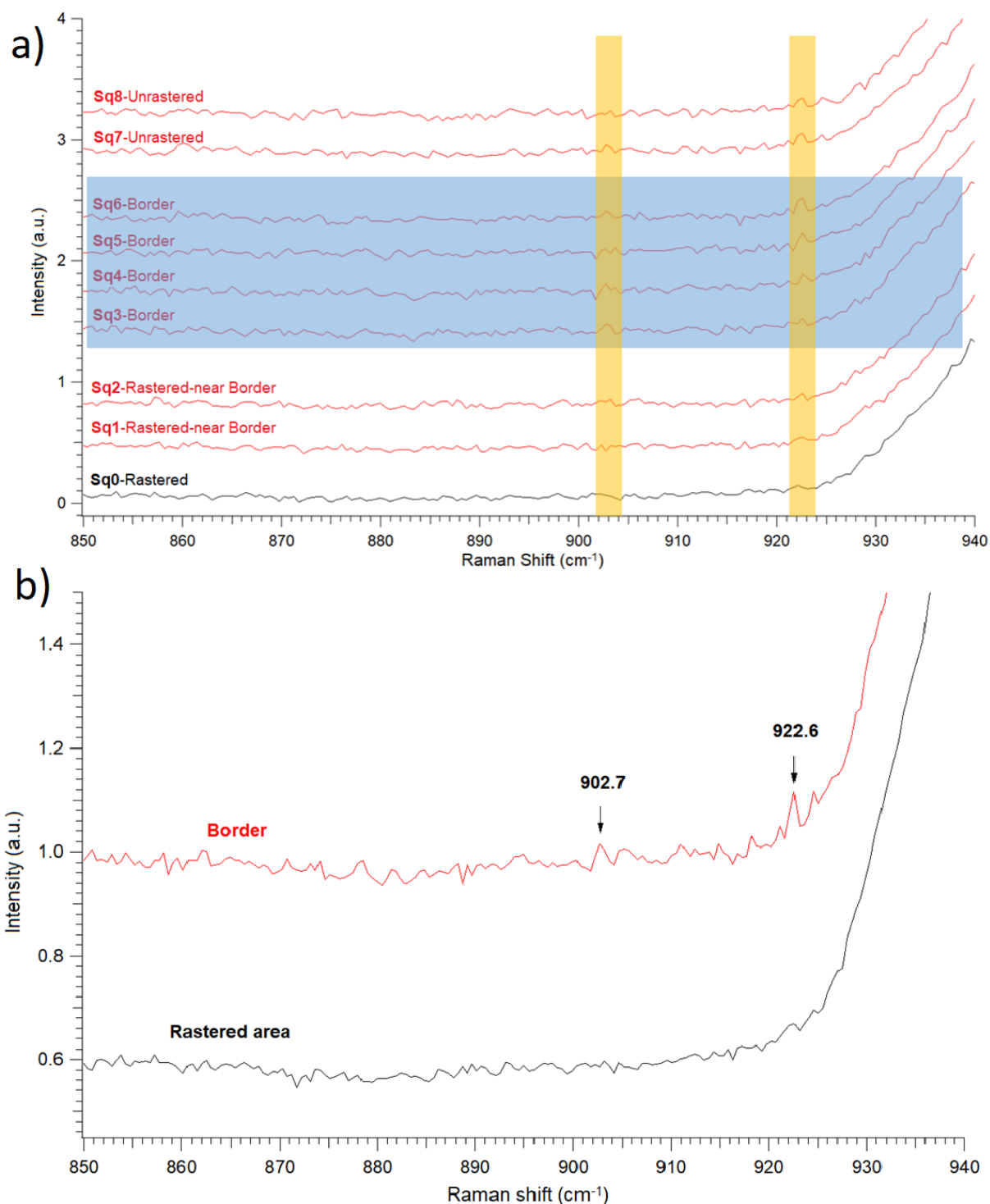**Fig. S9**. Averaged Raman spectra of (a) 2x2 and (b) 4x4 boxes in the Raman shifts between 850 to 940 cm^{-1}.

Discussion of the Raman data in Figs. S6-S9:

An area including a rastered MoS$_2$ crystalline surface and an unrastered MoS$_2$ zone with tentative Mo oxides was selected for a detailed Raman analysis. This area is depicted by a green box in Fig. S6(a) and its Raman map is in Fig. S6(b).

By a quick look on Fig. S6(b), one can only see slightly higher intensity on the unrastered vs. rastered zones, which comes from background difference arising after Si normalization. Individual Raman spectra were too noisy to observe any differences between rastered and unrastered zones. This is expected since an amount of tentative Mo oxides even at the border region is very small in comparison to strong presence of thick MoS_2 flake and Si in the Raman data. Therefore, we averaged several Raman spectra from the rastered and border regions in the map. This procedure helped us to increase the signal-to-noise (S/N) ratio and enhance visibility of any possible weak Raman peaks arising from the oxides. Figs. S7-9 show the average Raman spectra taken for 2x2 pixels in several places on the sample starting from rastered to unrastered regions. As can be noticed, there are some peaks – marked by yellow windows - from the border or near border regions, which are absent in the Raman spectra taken on the rastered area far away from the border. Furthermore, intensity of such new peaks is the highest at the border. Table S3 lists such peaks and their attributions.

For further enhancing the signal-to-noise ratio, average Raman spectra from zones with 4x4 pixels are shown in Figs. S7-9. There were obtained only in two cases: (i) on the rastered area far away from the border and (ii) on the border. Similar new peaks, which were observed from the 2x2 boxes in the border region, appear in the averaged Raman data from the 4x4 boxes. Furthermore, there are two new and faint peaks, namely at 425 and 493 cm^{-1} Raman shifts, which were absent in the data from 2x2 boxes, but can also be attributed to MoO_3 and MoO_{3-x}. They are marked in yellow in the Table S3 and were not included in the main paper. Generally all the peaks from 4x4 boxes appear smaller in comparison to the data from the 2x2 boxes. This is because increasing number of averaged pixels in each box indeed enhances the S/N ratio, but at the same time increases a collection area. The latter might diminish a contribution from single clusters.

Overall, quite many Raman peaks are listed in the Table S3 and discussed above, since they can be attributed to MoO_3 and MoO_{3-x} based on the literature data.

Table S3. Comparison MoO_{3-x}/MoO_3 Raman peaks obtained in this work with previous publications

Raman shift (cm^{-1})	Peak attribution	Raman shifts observed in literature (cm^{-1})
210	A_g-$\delta(OMo_2)$ in MoO_3 [1,2]	211,[2] 218,[1] 217.[3]
270	B_{2u} $\delta(O=Mo)$ in MoO_3 [1,4]	270,[1] 267

		(calculation)[4]
278	B_{1u}-δ(O=Mo) in MoO_3 [1,4] and MoO_{3-x} [2]	280, 282,[2] 270,[1] 276 (calculation)[4]
294	B_{3g} δ(O=Mo) in MoO_3 [1,4]	293,[2,5] 291,[1,3] 290 (calculation)[4]
356-359	B_{3u} δ(O=Mo) in MoO_3 [1,4] and MoO_{3-x} [2]	356,[2] 358,[1] 358 (calculation)[4]
425	MoO_{3-x} or MoO_2 [2,6]	422,[2] 423.[6]
461	B_{1g}-v($OMoO_3$) in MoO_{3-x} [2]	462,[2] 461[7,8]
493	m-MoO_2 in MoO_{3-x} or MoO_2 [2] In h-MoO_3 [9,10]	493,[2,11] 492,[9,10] 490.[2]
903	β-MoO_3 [12,13] m-MoO_3 [1] α-MoO_3 within MoO_{3-x} [14]	902.[1,12-14]
922-923	V(O=Mo) in α-MoO_3 hydrides[1,15] and hydrates[16] Mo-O_2 mode in MoO_{3-x} quantum dots[17]	922,[1,17] 923,[15] 920.[16]

Additional SEM-EDS and SEM-WDS investigations

First, we have performed additional SEM-EDS studies on the modified flake from Fig. 1 in the manuscript. Fig. S10 shows the SEM image and elemental mapping of the selected area which contain the border between rastered and unrastered areas. As seen, the agglomerated clusters at the border are visible in SEM image in Fig. S10(c). However, single clusters are invisible due to detection limits. The oxygen map in Fig. S10(f) shows quite clearly higher concentration of oxygen at the border in comparison to the MoS_2 surface.
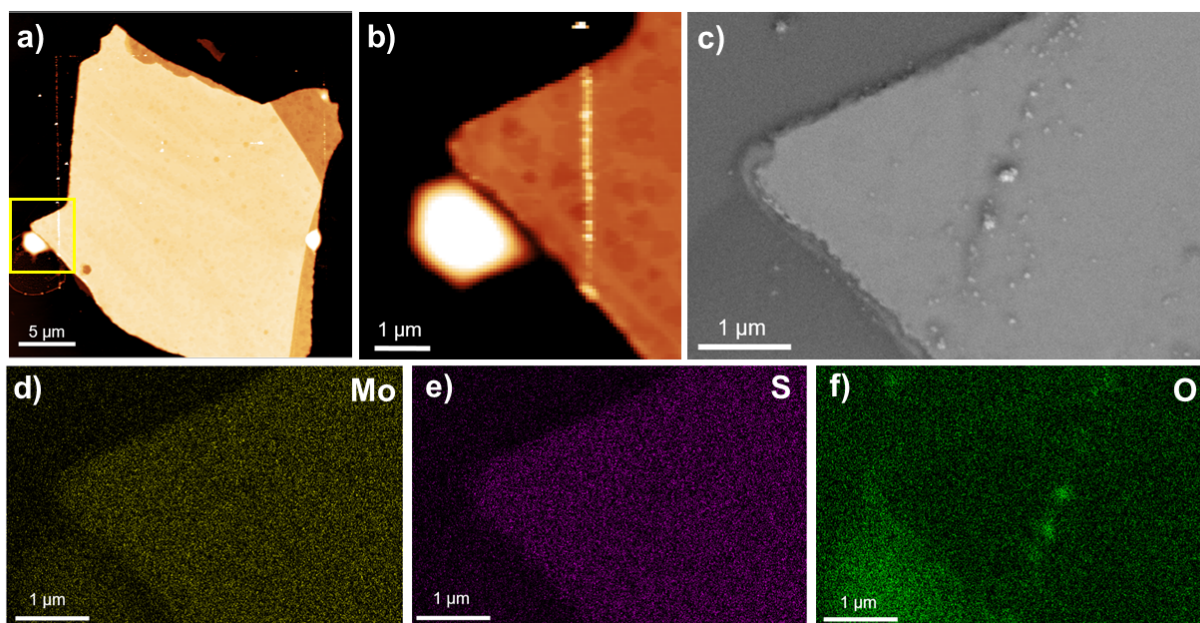
Figure S10. SEM-EDS analysis of the flake depicted in Fig. 1 in the main article: (a) Topography image of the whole flake after its rastering (32.7 nm Z-scale). (b) magnified topography image (23.9 nm Z-scale) of an area shown by yellow box in (a), depicting the border of the rastered area on the flake. In (a) and (b) brighter colors represent higher Z-values. (c) SEM image of the same area as in (b). (d-e) EDS elemental mapping for: (d) molybdenum (M series), (e) sulfur (K series) and (f) oxygen (K series).

We have also attempted a semi-quantitative SEM-EDS analysis of the oxygen, sulfur and molybdenum content and indeed observed an elevated oxygen content on the large agglomerated clusters accumulated near the border between rastered and unrastered regions, but quantifications and deconvolutions of the oxygen content with respect to Mo and S have showed to be unreliable. Some of the reasons could be that the bands of Mo and S coincide at ca. 2.3 keV and cannot be deconvoluted at low beam energies, which in turn are necessary to detect properly light elements such as oxygen. Nevertheless, we considered this issue further and used another SEM setup with WDS (wavelength dispersive X-ray spectroscopy) detectors. Therein, due to a beam size diameter of ca. 1 micron, we could not observe the signal from isolated clusters, but observed quite clearly the difference in oxygen content between rastered and unrastered zones, i.e., respectively, the portions of the samples with and without single MoO_x clusters. We present these SEM WDS results in the Table S4 below under rows: "New sample, rastered zone" and "New sample, unrastered zone". The new MoS_2 sample was freshly thermally etched at exactly the same conditions as described in the Experimental section of the manuscript.

Furthermore, we have also investigated the MoS_2 flake from Fig. 1 in the main paper (as well as Fig. S10 above), which is now ca. one year old. A comparisons between the

borderline region and rastered zones shows substantially higher oxygen content at the border, which follows the results in Fig. S10(f) and shows additional oxidation, which took place in the sample. See the data in Table S4, rows "Flake from Figs. 1 and S10, border region" and "Flake from Figs. 1 and S10, rastered region".

Finally, the silicon substrate with native silica film near the aforementioned flake was also measured to yield an amount of the oxygen present therein. This data is presented in a row "SiOx/Si substrate in the vicinity of the flake from Figs. 1 and S10" in Table S4. Due to the SEM WDS signal collected from substantial penetration depths and substantial Si percentage present in all the results in the Table S4, one might do the following estimates. First, to subtract the oxygen content originating from the silica interface. Second, to calculate Mo content within presumable MoO_x oxides present only atop MoS_2 surface based on average height comparisons between the largest oxide agglomerates of ca. 8 nm vs. the MoS_2 flake height of ca. 28 nm. In such a case, indeed the ratio of oxygen atop investigated MoS_2 sample to molybdenum within MoO_x clusters becomes even around 3.7. However, we treat such calculations with great caution and potentially faulty due to ageing of the sample as well as many other factors contributing to the penetration depth of the collected WDS signal.

To conclude, the SEM EDS and SEM WDS analyses did not provide unambiguous information about the stoichiometry of the MoO_x clusters discussed in the main paper, but showed the following results. First, the presence of isolated and sparsely present sub-nm MoOx clusters produced detectable increase in the O/Mo ratio (Table S4, rows 1-2). Second, agglomerated MoO_x clusters present at the border between rastered and unrastered zones displayed oxygen content pointing towards MoO_3, but other stoichiometries could not be excluded (Fig. S10 and Table S4, rows 3-5).

Table S4. Elemental analysis of the thermally etched MoS_2 samples provided by the EDS WDS measurements.

	O (at %)	Mo (at %)	S (at %)	Si (at %)	O/Mo ratio
New sample, rastered zone	0,8251	8,0982	16,9549	74,1218	0,1019
New sample, unrastered zone	1,0794	8,147	17,1757	73,598	0,1325
Flake from Figs. 1 and S10, border	3,8776	3,4133	6,6338	86,0754	1,1360

region					
Flake from Figs. 1 and S10, rastered region	2,0524	3,4408	6,9709	87,5359	0,5965
SiOx/Si substrate in the vicinity of the flake from Figs. 1 and S10.	1,2006	0	0	98,7994	Not defined

References

1   L. Seguin, M. Figlarz, R. Cavagnat and J. C. Lassègues, *Spectrochim. Acta Part A Mol. Biomol. Spectrosc.*, 1995, **51**, 1323–1344.

2   M. A. Camacho-López, L. Escobar-Alarcón, M. Picquart, R. Arroyo, G. Córdoba and E. Haro-Poniatowski, *Opt. Mater. (Amst).*, 2011, **33**, 480–484.

3   K. Eda, *J. Solid State Chem.*, 1992, **98**, 350–357.

4   M. A. Py and K. Maschke, *Phys. B+C*, 1981, **105**, 370–374.

5   P. A. Spevack and N. S. Mcintyre, *J. Phys. Chem*, 1992, **96**, 9029–9035.

6   B. B. Wang, X. X. Zhong, B. M. Ming, M. K. Zhu, Y. A. Chen, U. Cvelbar and K. Ostrikov, *Appl. Surf. Sci.*, 2019, **480**, 1054–1062.

7   B. B. Wang, X. X. Zhong, R. W. Shao, Y. A. Chen, U. Cvelbar and K. Ostrikov, *J. Phys. D. Appl. Phys.*, 2020, **53**, 415109.

8   Y. Li, X. Chen, M. Zhang, Y. Zhu, W. Ren, Z. Mei, M. Gu and F. Pan, *Catal. Sci. Technol.*, 2019, **9**, 803–810.

9   V. V. Atuchin, T. A. Gavrilova, V. G. Kostrovsky, L. D. Pokrovsky and I. B. Troitskaia, *Inorg. Mater. 2008 446*, 2008, **44**, 622–627.

10   S. Chen, Y. Dai, D. Zhao, al -, T. Allen Ebaugh, L. J. Bonville, R. Maric -, B. B. Wang, X. X. Zhong, R. W. Shao, E. Ghaleghafi and M. Bagher Rahmani, *Phys. Scr.*, 2022, **97**, 045811.

11   C. Prameela and K. Srinivasarao, *Int. J. Appl. Eng. Res.*, 2015, **10**, 9865–9875.

12   D. Liu, W. W. Lei, J. Hao, D. D. Liu, B. B. Liu, X. Wang, X. H. Chen, Q. L. Cui, G. T. Zou, J. Liu and S. Jiang, *J. Appl. Phys.*, 2009, **105**, 023513.

13   N. Illyaskutty, S. Sreedhar, G. Sanal Kumar, H. Kohler, M. Schwotzer, C. Natzeck and V. P. M. Pillai, *Nanoscale*, 2014, **6**, 13882–13894.

14   A. M. Hashem, S. M. Abbas, A. E. Abdel-Ghany, A. E. Eid, A. A. Abdel-Khalek, S. Indris, H. Ehrenberg, A. Mauger and C. M. Julien, *J. Alloys Compd.*, 2016, **686**, 744–752.

15   D. Liu, W. Lei, X. Chen, J. Hao, Y. Jin, Q. Cui and G. Zou, *J. Phys. Chem. B*, 2009, **113**, 16479–16482.

16   Y. Wang, M. Mayyas, J. Yang, M. B. Ghasemian, J. Tang, M. Mousavi, J. Han, M. Ahmed, M. Baharfar, G. Mao, Y. Yao, D. Esrafilzadeh, D. Cortie and K. Kalantar-Zadeh, *ACS Appl. Mater. Interfaces*, 2021, **13**, 53181–53193.

17   D. Ding, W. Huang, C. Song, M. Yan, C. Guo and S. Liu, *Chem. Commun.*, 2017, **53**, 6744–6747.